Wave-Coherent Airflow and Critical Layers over Ocean Waves

LAURENT GRARE, LUC LENAIN, AND W. KENDALL MELVILLE

Scripps Institution of Oceanography, La Jolla, California

(Manuscript received 12 March 2013, in final form 3 July 2013)

ABSTRACT

An analysis of coherent measurements of winds and waves from data collected during the Office of Naval Research (ONR) High-Resolution air–sea interaction (HiRes) program, from the *Floating Instrument Platform* (R/P *FLIP*), off the coast of northern California in June 2010 is presented. A suite of wind and wave measuring systems was deployed to resolve the modulation of the marine atmospheric boundary layer by waves. Spectral analysis of the data provided the wave-induced components of the wind velocity for various wind–wave conditions. The power spectral density, the amplitude, and the phase (relative to the waves) of these wave-induced components are computed and bin averaged over spectral wave age $c/U(z)$ or c/u_*, where c is the linear phase speed of the waves, $U(z)$ is the mean wind speed measured at the height z of the anemometer, and u_* is the friction velocity in the air. Results are qualitatively consistent with the critical layer theory of Miles. Across the critical height z_c, defined such that $U(z_c) = c$, the wave-induced vertical and horizontal velocities change significantly in both amplitude and phase. The measured wave-induced momentum flux shows that, for growing waves, less than 10% of the momentum flux at $z \approx 10$ m is supported by waves longer than approximately 15 m. For older sea states, these waves are able to generate upward wave-induced momentum flux opposed to the overall downward momentum flux. The measured amplitude of this upward wave-induced momentum flux was up to 20% of the value of the total wind stress when $C_p/u_* > 60$, where C_p is the phase speed at the peak of the wave spectrum.

1. Introduction

The air–sea interface is a complex system with surface waves interacting with the turbulent atmospheric and oceanic boundary layers over a wide variety of spatial and temporal scales. The surface waves span wavelengths ranging from millimeters to hundreds of meters, depending on the duration and magnitude of the wind forcing. The waves profoundly affect the exchange of momentum, mechanical energy, heat, and gases between the atmosphere and the ocean. Despite the fact that many theories have been developed and compared to experimental studies, there is still uncertainty about the parameterization of the wave growth and the modulation of the wind because of the presence of waves, the so-called wave-induced fluctuations. The spatial and temporal structure of the wave-induced airflow holds the key to the physics of wind–wave coupling, because it determines the pressure and shear stress distributions on the interface, and therefore the wave growth rate.

One of the leading theoretical treatments of the structure of the wave-induced flow fields was developed by Miles (1957), using a quasi-laminar approach where the viscous and turbulent Reynolds stresses were neglected. Later, these stresses were added to the model (Benjamin 1959; Miles 1959; Davis 1970; Miles 1993). The essence of the theory is that the height of a critical atmospheric layer z_c, directly influenced by the waves with phase speed c, is defined by $U(z_c) = c$, where $U(z)$ is the mean wind speed. According to the critical layer theory (CLT), the wave growth rate can be expressed through the values of vertical wave-induced velocity and the curvature of the mean wind profile both expressed at the critical height (CH).

Subsequent theoretical and numerical investigations include those of Townsend (1972), Gent and Taylor (1976), Chalikov (1978), Belcher and Hunt (1993), and Mastenbroek et al. (1996). These nonlinear models, based on the Reynolds-averaged equations, differ in the turbulence closure, and demonstrate sensitivity to the closure scheme. However the two-layer theory suggested by Townsend (1972), advanced by Belcher and Hunt (1993), and numerically modeled by Mastenbroek et al. (1996), significantly differs from the Miles theory. Here, the

Corresponding author address: W. Kendall Melville, Scripps Institution of Oceanography, 9500 Gilman Dr., La Jolla, CA 92093-0213.
E-mail: kmelville@ucsd.edu

DOI: 10.1175/JPO-D-13-056.1

waves generate perturbations of the turbulent stresses in a thin region close to the surface (the inner region with depth L_i), which produces an asymmetry of the streamlines around the wave crest (the so-called nonseparated sheltering), with a thickening of the inner region in the lee face of the waves. This asymmetry generates a shift of the surface pressure that leads to the transfer of energy between the wind and the waves through the work of the form drag. Further analysis of both the nonseparated sheltering mechanism and the Miles theory (Belcher and Hunt 1998) led to the classification of the coupling between the airflow and water waves into three parameter regimes based on the wind forcing, the thickness of the inner layer, and the location of the critical layer. For slow waves ($c/u_* \lesssim 15$), of wavenumber k, the critical layer lies within the thin ($kL_i \ll 1$, $z_c < L_i$) inner region; for intermediate waves ($15 \lesssim c/u_* \lesssim 25$), the inner region is thick ($kL_i \sim 1$) and its depth is of the same order of magnitude as the critical height ($L_i \sim z_c$); and for fast waves ($c/u_* \gtrsim 25$), the inner region is thin ($kL_i \ll 1$) and the critical height is far above the surface ($kz_c \gg 1$). According to Belcher and Hunt (1998), for slow and fast waves, the critical layer does not play any dynamical role and the momentum transfer between the wind and the waves is controlled by the nonseparated sheltering in the inner region. For intermediate waves, the detail of the interaction between the inner region and the critical layer remains unclear.

Over recent decades, the development of direct numerical simulation (DNS) and large-eddy simulation (LES) has provided new insights into the interaction between wind and waves. Sullivan et al. (2000) and Kihara et al. (2007) have performed DNS of the airflow above idealized slow and intermediate waves. They gave a detailed description of the airflow, showing the effect of the critical layer with a change of phase of the wave-induced velocities and a change of sign of the wave-induced momentum flux at the critical height.

Although the numerical models (Reynolds-averaged Navier–Stokes equations, DNS, and LES) are able to provide various descriptions of the flow over waves, they generally simulate the wavy interface by monochromatic steady Stokes waves. One-dimensional (z) models developed by Makin et al. (1995), Makin and Kudryavtsev (1999), and Hara and Belcher (2002) parameterize the coupling between wind and waves over a wave field described by directional wave spectra. These models, applicable for developing and for fully developed seas, estimate the surface wave-induced momentum flux and therefore the wave growth rate for all scales of the wave field. Similarly, Sullivan et al. (2010) have performed LES simulations of the airflow above an empirical 3D-propagating surface wave field with the idea of using a measured wave field in the future. This may turn out to be one of the most productive ways to compare field measurements and numerical simulations.

The theories and numerical models detailed above are mainly focused on wind-driven waves; that is, young and growing seas. However, numerical simulations of Cohen and Belcher (1999), Makin (2008), Hanley and Belcher (2008), and Sullivan et al. (2008, 2010) were developed for wave-driven wind cases. The results are in qualitative agreement with the observations of Grachev and Fairall (2001) and Smedman et al. (1999, 2009). When the wind is following fast-moving swell, waves in the vicinity of the peak in the swell spectrum produce an upward momentum flux, which can extend over large vertical scales and exceed the downward turbulent momentum flux.

Many measurements have been performed to test the ability of the CLT to predict the wave-induced airflow and the growth rate of the waves. Direct measurements of the growth rate of waves forced by the wind in a channel were conducted by Bole and Hsu (1969), Wilson et al. (1973), Mitsuyasu and Honda (1982), Peirson and Garcia (2008), and Grare et al. (2013). Laboratory and field measurements of the airflow above waves, which gave descriptions of the wave-induced components of the wind and momentum fluxes, were performed in a channel by Kato and Sano (1969), Stewart (1970), Lai and Shemdin (1971), Hsu et al. (1981), Hsu and Hsu (1983), Papadimitrakis et al. (1984), Mastenbroek et al. (1996), and in the field by Kondo et al. (1972), Davidson and Frank (1973), and Antonia and Chambers (1980). More recently, Hristov et al. (2003) have presented field measurements of wave-induced wind components which were in agreement (in both amplitude and phase) with the Miles theory for wave ages c/u_* in the range 16–40 and for wind speeds up to $13\,\mathrm{m\,s^{-1}}$. Furthermore, measurements of the pressure field above waves to quantify the wind energy input were conducted by Shemdin and Hsu (1967), Papadimitrakis et al. (1986), Savelyev et al. (2011), and Grare et al. (2013) in the laboratory, and by Dobson (1971), Snyder et al. (1981), Hsiao (1983), Hasselmann and Bosenberg (1991), and Donelan et al. (2006) in the field. Plant (1982) collated both laboratory and field data available at that time and through a simple relationship related the growth rate of waves β to the reciprocal of the wave age u_*/c.

Laboratory measurements are useful to give a fine and detailed description of the physical processes that occur in the coupling of the wind and the waves, but they are limited by the narrow-banded wave field. In this context, accurate and reliable field observations over the open ocean are most valuable as they reflect the complex wind–wave interaction acting over a large range of scales.

In the present paper, we present results from field experiments that show that the critical layer plays an important role in the structure of the airflow, with a sharp change of phase of the wave-induced velocities across the critical height, accompanied by a reduction of the amplitude of the wave-induced velocities. The measured contributions of the wave-induced momentum flux to the wind stress show that, for growing waves, less than 10% of the downward momentum flux is supported by waves with wavelengths longer than approximately 15 m. On the contrary, for old sea states, waves longer than approximately 15 m are able to generate upward momentum flux, with intensity levels that can represent up to 20% of the wind stress. In section 2, we summarize the experimental setup. In section 3, we present the measurements of the wave-induced velocities in the airflow and the influence of the critical height that provide the basis for the results presented here. In section 4, we present the dependence of the contribution to the wind stress of the wave-induced momentum flux integrated over all scales as a function of the wave age C_p/u_*, based on the phase speed at the peak of wave spectrum C_p. The dependence is also studied in the frequency domain. Finally, in section 5, we discuss the implications of these findings.

2. Experiment

The measurements described here were taken aboard the *Floating Instrument Platform* (R/P *FLIP*) moored approximately 25 km off the coast of northern California (38°20.14′N, 123°25.40′W), in 160-m deep water during 7–20 June 2010. Two eddy covariance systems (ECSs) and a laser wave gauge were deployed at the end of the starboard boom approximately 18 m from the hull. The lower and upper ECSs were located approximately 7.5 and 10.5 m above mean sea level (MSL), respectively, while the laser wave gauge was set about 8.5-m MSL. The wave gauge was 2 m outboard and 1.4 m downwind of the horizontal location of the ECSs (Fig. 1).The effect of this horizontal shift between the ECSs and the wave gauge was taken into account in the computation of the phase shift between the velocity fluctuations and the surface elevation.

The wave gauge, a single point laser altimeter [Riegl LD90-3100-Extremely High Speed (EHS)], measured the distance to the water surface at 12 kHz (averaged down to 20 Hz) with a footprint of approximately 5-cm diameter. Each ECS acquired meteorological and boundary layer flux data. Each of the two ECSs included a three-axis sonic anemometer–thermometer (Campbell CSAT3) and an open-path infrared (IR) hygrometer–CO_2 sensor (LI-COR 7500). A relative humidity–temperature probe (Vaisala HMP45) located close to the upper ECS was also used to provide reference

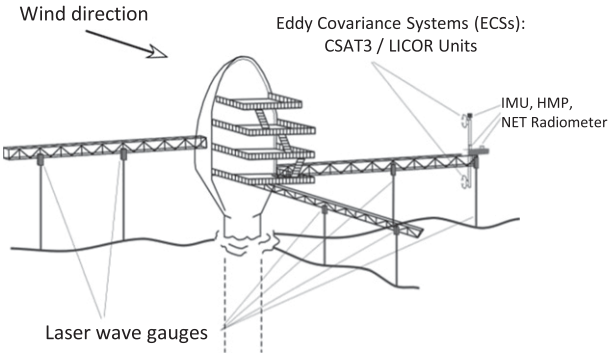

FIG. 1. Experimental setup on R/P *FLIP*.

values of humidity and temperature. A net radiometer (CNR1) was used to measure the energy balance between incoming short- and longwave IR radiation versus surface-reflected short- and outgoing longwave IR radiation. A 6-degree-of-freedom inertial measurement unit [IMU; MEMSIC Attitude Heading Reference System (AHRS) 400] located about 50 cm away from the upper ECS provided the attitude and acceleration of the sensors. These instruments were sampled at 20 Hz.

The sonic temperature was corrected for humidity and pressure, and the latent heat flux was corrected for density variations (Webb et al. 1980). The sonic velocities and the surface displacements were corrected to account for the motion of R/P *FLIP* using the acceleration components, the rate angles, and the attitude angles measured by the IMU (Edson et al. 1998). An example of the spectra of surface displacement (measured by the laser wave gauge) and corrections applied is shown in Fig. 2. In both the spectrum of the vertical displacement of the sensors (black dashed line) and the spectrum of the distance between the surface and the wave gauge (gray solid line), two peaks appear at about 0.02 and 0.04 Hz, which are due to the tilt and heave motion of R/P *FLIP*, respectively (Smith and Rieder 1997). As pointed out in Edson et al. (1998), the computation of displacement through the integration of the acceleration is not possible for low frequencies because of the drift of the accelerometer. Thus, the slow motion (periods greater than 80 s) of the instruments was assumed to be mainly due to the roll and tilt of R/P *FLIP* and was computed using the attitude angles and velocity outputs of the IMU that are corrected internally for drift. After corrections, the two frequency peaks do not appear in the spectrum of the wave displacement (black solid line), and the tail of the frequency spectrum follows a well-known -4 slope up to almost 2 Hz. At higher frequencies, the tail of spectrum deviates from the -4 slope, because the smallest scales of the wave field are not resolved by the laser wave gauge. The wind velocities and the sonic temperature were

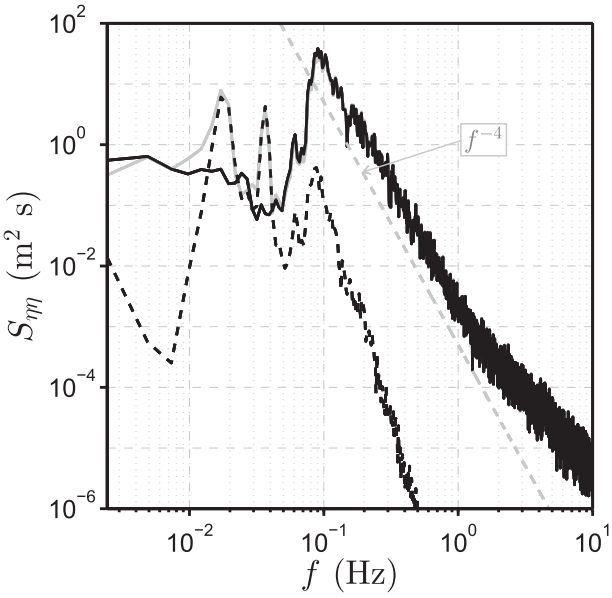

FIG. 2. Spectra of surface elevation for a 30-min record starting at 0830 UTC 15 Jun 2010. Gray solid line is the signal from the laser wave gauge after despiking. Black dashed line is the vertical displacement of the wave gauge computed from IMU. Black solid line is the final sea surface displacement spectrum after motion compensation. Gray dashed line has a −4 slope.

despiked to remove the largest outliers in the signals. Then, the wind velocities were corrected to account for the motion of R/P *FLIP* in a range of frequencies from 0.0125 Hz (80-s period) up to 3 Hz. Above 3 Hz, high-frequency vibrations were detected in the spectrum of the acceleration recorded by the IMU. These vibrations were probably due to resonant modes of the pole supporting the ECSs and the IMU. No corrections were applied above 3 Hz to avoid adding any coherent fluctuations in the wind speed components. Moreover, the cumulative sum of the cospectrum between the horizontal and vertical components of the wind showed that more than 97% of the wind stress was supported by frequencies below 2 Hz. In that context, turbulent fluxes of momentum, heat, and water vapor were computed using the covariance method by spectral summation of the cospectrum with frequencies up to 2 Hz. After corrections, the velocity was projected onto a frame of reference aligned either with the mean direction of the wind or with the mean direction of propagation of the dominant waves. In both cases, the projection ensures that the mean vertical velocity is zero over 30-min segments of data. Mean values, fluxes, and spectral analysis were computed over the same 30-min records. This time window ensures sufficient statistical reliability in the wind stress and spectral estimates. To limit the effects of nonstationarity on the values of the fluxes, linear trends in the wind velocity were removed before the computation of the fluctuations. Auto- and cross-spectra were computed on the 20-Hz data in the 30-min segments using 2048-point fast Fourier transforms (FFTs) to provide spectra over 102.4 s with a frequency resolution of 0.0097 Hz.

The wave direction was determined through the directional spectra of the surface displacement measured by an array of five laser wave gauges [MDL Industrial Laser Module (ILM) 500] located on the starboard, port, and face booms of R/P *FLIP* (Fig. 1). These laser wave gauges were also corrected to account for the motion of R/P *FLIP*. For each 30-min record, the directional spectrum was computed using the Wave Analysis for Fatigue and Oceanography (WAFO) toolbox of MATLAB routines (WAFO-Group 2000). The distances between wave gauges range from 8 to 35 m, therefore resolving directional spectra for waves with frequencies up to about 0.2 Hz [Massel and Brinkman (1998), their Eq. (36)]. For the dataset analyzed, the peak frequency of the surface wave spectrum remains at less than 0.15 Hz, meaning that the spatial distribution of the wave gauges on R/P *FLIP* provides enough spatial resolution to resolve the dominant wave direction within ±5°.

Figure 3 shows the evolution of the main parameters of the marine atmospheric boundary layer (MABL) during the High-Resolution air–sea interaction (HiRes) experiment when most of the instruments were deployed. The x axis represents the date in days during 11–19 June 2010, using the coordinated universal time (UTC). Data points are 30-min averages.

Figure 3a shows the mean wind speed at 10 m U_{10}, the wind direction, and the direction of propagation of the dominant waves. Here, U_{10} was computed assuming a constant flux layer with a logarithmic wind profile:

$$U_{10} = U(z = 10) = U(z_1) + \frac{u_*}{\kappa} \ln\left(\frac{10}{z_1}\right), \qquad (1)$$

where u_* is the friction velocity and $U(z_1)$ is the wind speed measured at the height z_1 of the upper anemometer and κ is the von Kármán constant set to 0.4. It shows that most of the time, the wind speed was greater than 10 m s^{-1} except for two periods on 12 and 13 June 2010. An abrupt change of wind direction is associated with the drop in the wind speed that occurred on 13 June. The main direction of the waves remained quite constant except at the beginning of the experiment and for a short period of time during 13 June. Thus, the shift in direction between the wind and the waves remained less than 20° except on 11 June when it reached 40° and on 13 June where the wind is almost opposed to the waves for a 4-h period.

Figure 3b shows the significant wave height measured from the laser wave gauge and the wave age C_p/U_{10}.

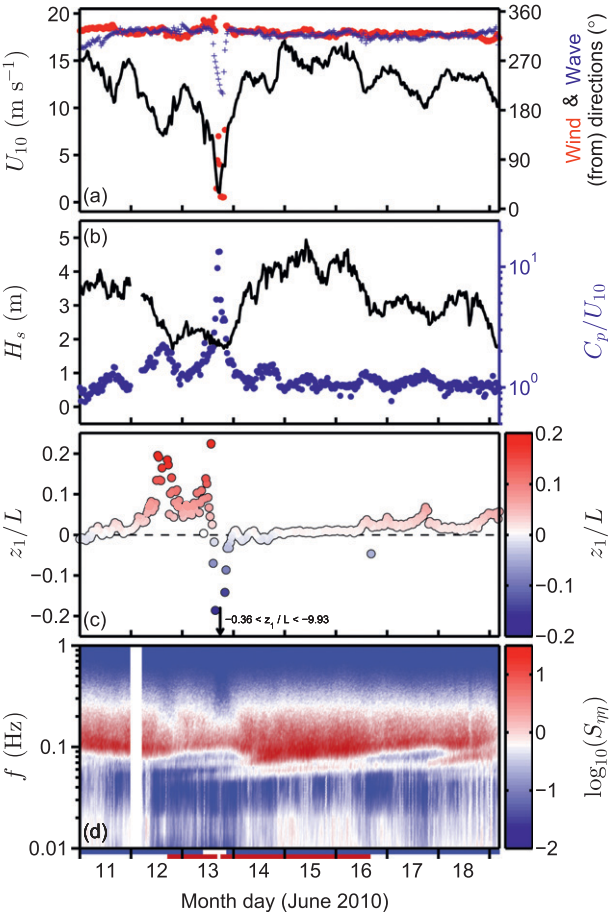

FIG. 3. (a) U_{10} (black line), wind direction (red dots), and direction of propagation of the dominant waves (blue crosses). (b) Significant wave height (black line) and wave age C_p/U_{10} (blue dots). (c) Stability parameter z_1/L, where $z_1 \approx 10.5$ m is the height of the upper ECS and L is the Monin–Obukhov length. (d) Spectrogram of the surface displacement. All data points are 30-min averages. Blue and red thick lines along the x axis of (d) represent the periods of time when the upper and lower ECSs were fully operational, respectively.

Except on 13 June, the wave age remained between 0.8 and 2.0, which is representative of a mature sea. In contrast, on 13 June, the wave age increased up to 20, which is representative of conditions because of swell and light local winds.

Figure 3c shows the evolution of the stability parameter z_1/L, where L is the Monin–Obukhov length (Monin and Obukhov 1954), and z_1 is the height of the upper ECSs MSL. Here, L was computed from the sensible heat flux and the friction velocity u_* measured by the upper ECS ($z_1 \approx 10.5$ m):

$$L = -\frac{u_*^3 \overline{\theta}_v}{\kappa g \overline{w'\theta'_v}}, \tag{2}$$

where θ_v is the virtual temperature, g is the gravity, and the overbar represents an average with respect to time. It shows that, most of the time, stable conditions ($z/L > 0$) were encountered. A short period of unstable conditions is associated with the declining wind speed. Furthermore, except for the period from the beginning of 12 June to the end of 13 June, quasi-neutral conditions were encountered. The range reported on the lower part of the plot on 13 June corresponds to an unstable period of time for which the stability parameter was out of the range of the graph.

Finally, Fig. 3d shows the spectrogram of the surface displacement. For this figure only, the spectra were computed using 4096-point FFT windows. It shows that the frequency of the wave peak remained between 0.08 and 0.15 Hz. Also shown is the superposition of wind waves and swell, especially at the end of the experiment, on 18 June. The lack of data at the beginning of 12 June is due to laser-wave-gauge failure.

In Fig. 3d, the blue and red thick lines along the x axis show the time when the upper and lower ECS were fully operational, respectively. For the lower ECS, at the beginning (until 1630 UTC 12 June) and the end of the experiment (from 1630 UTC 16 June), poor connections generated large spikes in the signals from the sonic anemometer and thermometer. For a short period of time (from 1630 to 1800 UTC 13 June), large fluctuations, not correlated with the waves, were present in the velocity signals. They generated abnormally high values of the velocity correlations. For these periods of time, data from the lower ECS were excluded from the following analysis. For the upper ECS, during a 10-h period, starting at 1000 UTC 13 June, small spikes were present in the velocity and temperature data. These spikes were presumably generated by dry residues of accumulated salt. Despite this, the values of the mean speed and the fluxes remained in good agreement with those from the lower ECS. These data were removed from the following analysis (except for Fig. 3 and Fig. 5).

Figure 4a shows a comparison between the neutral drag coefficient $C_{D_{10n}}$ computed from both the upper (blue open circles) and the lower (red open circles) ECSs, and that calculated with the bulk parameterization from the Tropical Ocean and Global Atmosphere Coupled Ocean–Atmosphere Response Experiment (TOGA COARE) 3.0 algorithm (Fairall et al. 2003). The 95% confidence intervals for the bin-averaged points are computed following Bendat and Piersol (2010):

$$\hat{a} - t_{(N,0.05)}\frac{\sigma}{\sqrt{N}} \le a \le \hat{a} + t_{(N,0.05)}\frac{\sigma}{\sqrt{N}}, \tag{3}$$

where N is the number of samples per bin, $\hat{a}$ is the bin-averaged estimate, σ is the standard deviation, and $t_{(N,\,0.05)}$

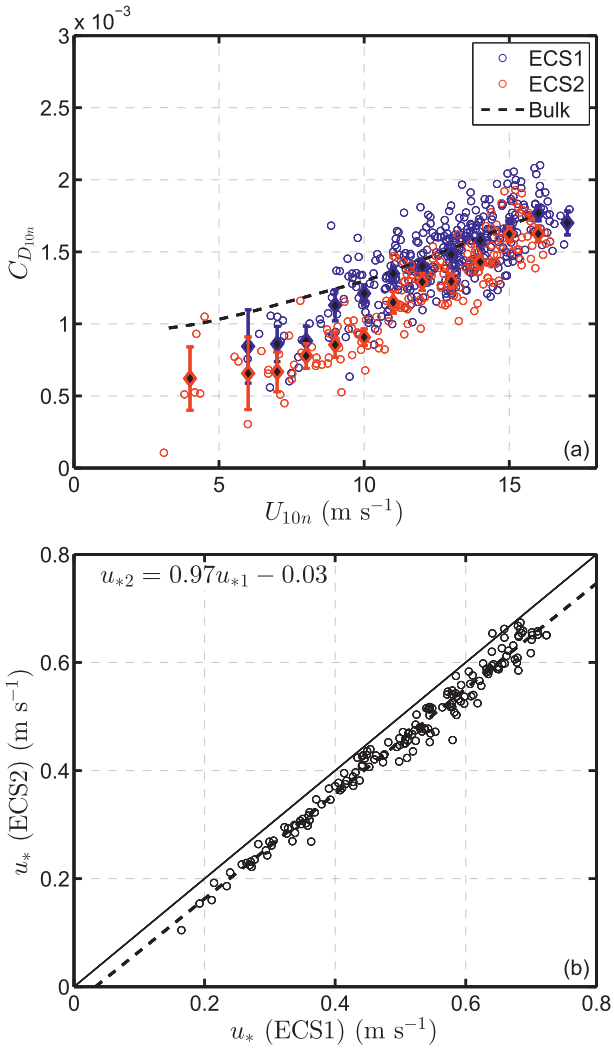

FIG. 4. (a) $C_{D_{10n}}$ as a function of U_{10n} measured by the two ECSs (blue and red open circles) compared to the TOGA COARE 3.0 (Fairall et al. 2003) bulk algorithm (dashed line). Solid diamonds are bin-averaged data with their corresponding 95% confidence intervals for each ECS. (b) Direct comparison u_* measured by ECS1 ($z_1 \approx 10.5$ m) vs ECS2 ($z_2 \approx 7.5$ m). The equation $u_{*2} = 0.97u_{*1} - 0.03$ is the linear fit to the data.

is the value of the t distribution at 95% for N samples. The neutral drag coefficient is expressed as follows:

$$C_{D_{10n}} = (u_*/U_{10n})^2, \tag{4}$$

where U_{10n} is the neutral wind speed at 10 m:

$$U_{10n} = \frac{u_*}{\kappa}\log\left(\frac{10}{z_0}\right). \tag{5}$$

The roughness length z_0 is calculated assuming a logarithmic profile of the wind speed corrected for the effects of buoyancy:

$$z_0 = \frac{z_i}{\exp\left[\dfrac{\kappa U(z_i)}{u_*} + \Psi_m(z_i/L)\right]}, \tag{6}$$

where Ψ_m is a universal function related to the dimensionless velocity gradient (Panofsky 1963), and z_i is the height of the ECS.

For the most of the data, the agreement is good, especially when the wind speed is greater than 10 m s^{-1}. Below 10 m s^{-1}, the variability of the drag coefficient increases and the TOGA COARE 3.0 parameterization gives higher values than measured. However, the data points that correspond to wind speeds smaller than 10 m s^{-1} are associated with the two extrema of the wave age observed in Fig. 3b on 12 and 13 June, which characterize local light wind blowing over long waves. Smedman et al. (2003, 2009) and Högström et al. (2013) have shown that, for low wind speeds, fast waves can generate wave-coherent structures in the airflow that invalidate the Monin–Obukhov scaling. They also showed a considerable scatter of the drag coefficient ($0.5 < 10^3 C_D < 1.5$) in the range $3 < U_{10} < 10$ m s^{-1} [Smedman et al. (2003), their Fig. 10]. Nevertheless, as indicated by the bin-averaged data, the values of the drag coefficient from the lower ECS are systematically lower than those measured by the upper ECS. To parameterize this difference, direct comparison of the friction velocity measured by the two ECSs have been reported in Fig. 4b. This plot shows that the friction velocity measured by the lower ECS (ECS2) is consistently lower than that measured by the upper one (ECS1). The linear fit of the data gives a linear coefficient of 0.97 with an offset of -0.03 m s^{-1}, and the averaged ratio u_*(ECS2)/u_*(ECS1) is equal to 0.903. The data show that on average the friction velocity in the range (7.5, 10.5) m MSL is constant to within 10%. The generally good agreement between our data and the bulk parameterization at high wind speeds, and the agreement of our data with those from Smedman et al. (2003) at low wind speed, implies that our covariance measurements were consistent with other field data.

3. Wave-induced velocities

Figure 5 shows the evolution over 8 days of the phase shift and the squared coherence between the surface displacement and the horizontal velocity (Figs. 5a,c), and between the surface displacement and the vertical velocity (Figs. 5b,d) as a function of the frequency f and the phase speed of the waves $c = g/2\pi f$. Hereinafter, the horizontal velocity u is defined as the component of the wind aligned with the direction of propagation of the dominant waves. The phase shift $\Phi_{\eta u_i}$ between the velocity u_i (where $u_1 = u$ is the horizontal component and

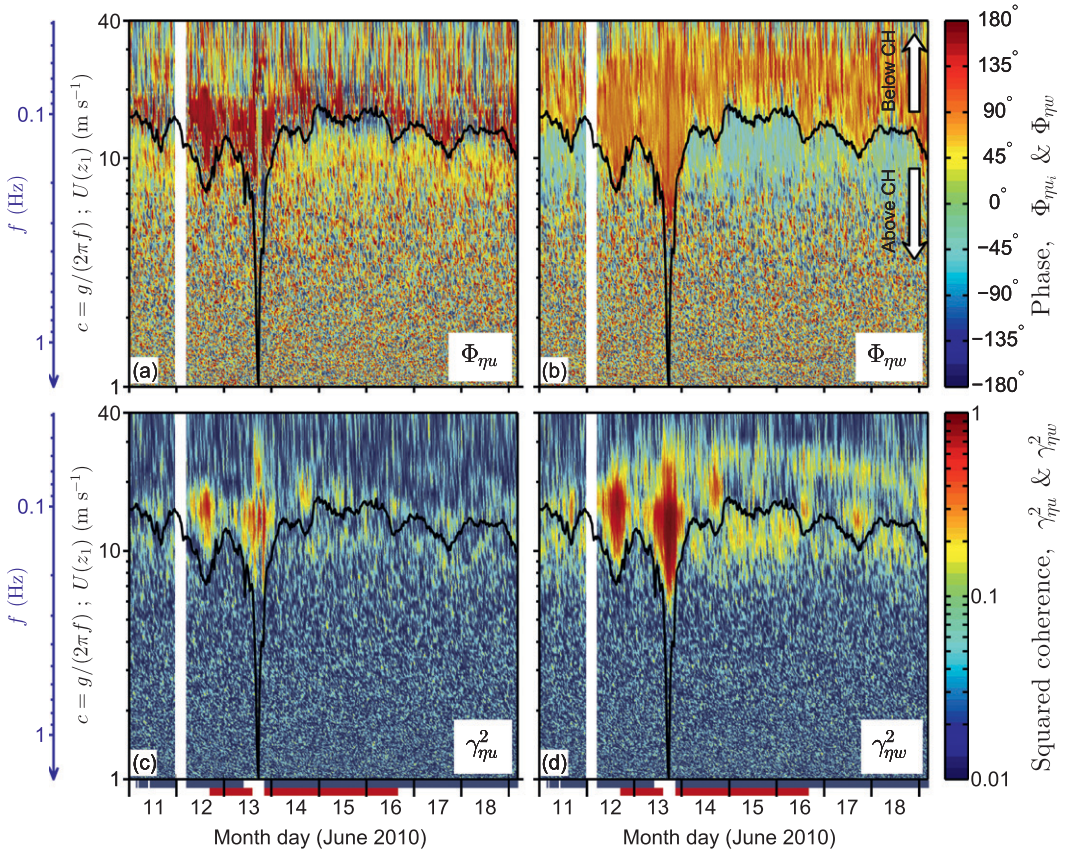

FIG. 5. (a) $\Phi_{\eta u_i}$ and (c) $\gamma^2_{\eta u}$ between the surface displacement and the horizontal velocity (along the direction of propagation of the dominant waves). (b) $\Phi_{\eta u_i}$ and (d) $\gamma^2_{\eta w}$ between the surface displacement and the vertical velocity. A positive phase shift means the waves lead the velocity fluctuations. Velocities were recorded by the upper ECS at $z_1 \approx 10.5$ m. The leftmost y axis is the frequency. The other y axis is the linear phase speed of the waves $c = g/2\pi f$. The black line shows $U(z_1)$ at the height of the ECS and also corresponds to the phase speed of waves for which the ECS is at their critical height.

$u_3 = w$ is the vertical component) and the surface displacement η is the argument of the complex cross-spectral density function $S_{\eta u_i}$ between η and u_i:

$$\Phi_{\eta u_i} = \arg(S_{\eta u_i}). \tag{7}$$

A positive phase shift means the waves lead the velocity fluctuations.

The horizontal distance between the anemometers and the wave gauge Δx is taken into account in the computation of the phase shift, assuming a linear decomposition of the wave field, as follows:

$$(\Phi_{\eta u_i})_{\text{corrected}} = (\Phi_{\eta u_i})_{\text{measured}} + \frac{\Delta x(360)}{\lambda}, \tag{8}$$

where $\lambda = 2\pi c^2/g$ is the wavelength of the waves with phase speed c.

The squared coherence $\gamma^2_{\eta u_i}$ between the velocity u_i and the surface displacement η is defined as

$$\gamma^2_{\eta u_i} = \frac{|S_{\eta u_i}|^2}{S_{\eta\eta} S_{u_i u_i}}, \tag{9}$$

where $|S_{\eta u_i}|^2$ is the squared magnitude of the cross-spectral density, and $S_{\eta\eta}$ and $S_{u_i u_i}$ are the auto-spectral densities of the surface displacement and the velocity, respectively.

Figures 5a and 5b show that for both components of the wind, there is an abrupt change of phase when the wind measurement is at the critical height of the waves. For waves traveling faster than the wind speed at the elevation of the instrument, the anemometer is below the critical height of these waves. The phase shift tends toward the bounds defined by the potential theory, which are 180° for the horizontal component u and 90° for the vertical component w. For waves that propagate slower than the wind, the anemometer is above their critical heights, and the phase tends toward bounds that depend on the value of c/u_* according to the CLT. For these

waves, the phase is between 0° and 90° for the horizontal velocity and around −45° for the vertical velocity. These results are consistent with the results of Stewart (1970) and Hristov et al. (2003) even when the wind speed was up to 18 m s^{-1} and the significant wave height H_s was up to 5 m.

Figures 5c and 5d show that the wind components are coherent with waves having phase speeds between 5 and 30 m s^{-1} ($0.3 \gtrsim f \gtrsim 0.05$ Hz). The levels of (squared) coherence are greater for the vertical than for the horizontal velocity. For waves traveling faster than the wind, coherent fluctuations of the velocities are always present and the level of coherence increases when the wind speed decreases, whereas for waves propagating at a phase speed lower than the wind speed, coherent fluctuations appear only during high wind conditions ($U > 10$ m s^{-1}). Furthermore, although it is not obvious in the figure, there is a drop off of the coherence between the velocities and the waves when the phase speed is equal to the mean wind speed. This behavior is in agreement with the CLT.

To study the evolution of the phase shift and the amplitude of the wave-induced velocities with the spectral wave age $c(f)/U$, where $c(f) = g/2\pi f$, we have selected fluctuations of the velocity coherent with the waves in a way similar to that used by Hare et al. (1997). This selection has been done according to the level of coherence between the surface elevation and the velocities. To minimize the effect of spurious noise and to ensure sufficient wave-induced signals, only the frequencies for which the squared coherence $\gamma^2_{\eta u_i}$ was above a threshold of 0.1 were included in the final dataset. We also restricted the selection to frequencies higher than 0.05 Hz to neglect wind fluctuations that could be correlated with the heave (around 0.04 Hz) and tilt motions (around 0.02 Hz) of the R/P *FLIP* and that do not represent physical coupling between the airflow and the wavy surface. We also removed data corresponding to cases where the wind is not aligned with the waves to minimize the directional effects. Thus the selected data were restricted to cases where the angle between the wind and the dominant waves is less than 30°. As mentioned earlier, the cases with erroneous measurements were excluded from the analysis. Periods of time with reliable measurements performed where the wind was aligned with the waves (within ±30°) are encapsulated into the x axis of Figs. 5c and 5d with the blue and red patches corresponding to the upper and lower ECSs, respectively.

The spectral functions such as the wind–wave phase shift $\Phi_{\eta u_i}$, the squared coherence $\gamma^2_{\eta u_i}$, and the cross-spectral density $S_{\eta u_i}$ between the surface displacement and the velocity fluctuations, were obtained from FFTs over 30-min records. The mean wind speed $U(z_i)$, the friction velocity u_* and the mean height z_i of the ECS MSL, averaged over the same 30-min samples are associated with each of those spectral functions. The spectral functions ($\Phi_{\eta u_i}$, $\gamma^2_{\eta u_i}$, $S_{\eta u_i}$, and their derivatives) are presented in the following sections as a function of the wave age $c(f)/U$. We use the mean wind speed $U = U(z_i)$ measured at the height z_i of each ECS to highlight the influence of the critical height on the wave-induced airflow. With these representations, when the ratio c/U is larger (smaller) than unity, it means that measurements were taken below (above) the critical height z_c of waves traveling at the phase speed c. Nonetheless, for comparison with other studies, as the heights of the ECSs were 7.5 ± 0.6 and 10.5 ± 0.6 m, respectively, these mean wind speeds $U(z_i)$ are almost equal to the classical wind speed at 10 m (U_{10}). Indeed, for the entire experiment, the wind speed U_{10} remains within ±0.25 m s^{-1} (±0.5 m s^{-1}) of the mean wind speed measured by the upper (lower) ECS.

Figure 6 shows the distribution of the number of occurrences, which satisfy the selection criteria described above, as a function of the bin-averaged spectral wave ages c/U and c/u_*. The width of the bins of the wave ages is equal to 0.1 for c/U and 2 for c/u_*. For the squared coherence between the wave displacement and the vertical velocity above the threshold of 0.1 ($\gamma^2_{\eta w} > 0.1$), 4350 points were included in the bin averaging. Only 2035 points were included in the bin averaging if the squared coherence between the wave displacement and the horizontal velocity is above the threshold of 0.1 ($\gamma^2_{\eta u} > 0.1$). The difference in the number of points included in the averaging supports the feature previously observed in Figs. 5c and 5d: the wave signature in the atmospheric boundary layer is stronger for the vertical fluctuations than for the horizontal. Furthermore, Fig. 6 shows distinct bimodal distributions with a minimum occurring for waves which propagate at the mean wind speed recorded by the anemometer; that is, for waves with the anemometer at their critical height. When the phase speed c is normalized by u_*, the minimum is reached around $c/u_* \sim 25$–30. This type of distribution is evidence that the amplitude of the wave-induced velocities drops off at the critical height.

In Fig. 7, the variations of the phase shift between the waves and both horizontal (Fig. 7a) and vertical (Fig. 7b) fluctuations of the wind are shown as a function of the spectral wave age c/U for the assembled dataset. In Fig. 7c, the difference between these two phase shifts is shown, and only data points for which both $\gamma^2_{\eta u} > 0.1$ and $\gamma^2_{\eta w} > 0.1$ are reported (896 points). The bin-averaged 95% confidence intervals are calculated following the method described in Bendat and Piersol (2010) as follows:

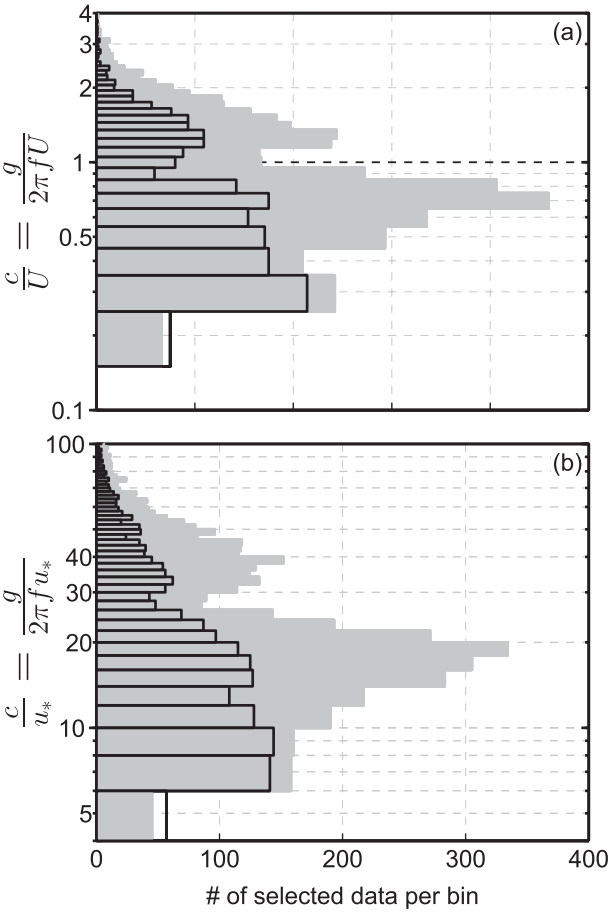

FIG. 6. Distribution of the number of points that fit the selection criteria per wave age bins (a) c/U and (b) c/u_*. Gray solid bars present the distributions of selected points for which $\gamma^2_{\eta w} > 0.1$. Black open bars present the distributions of selected points for which $\gamma^2_{\eta u} > 0.1$. The size of the bins is 0.1 for the wave age c/U and 2 for the wave age c/u_*.

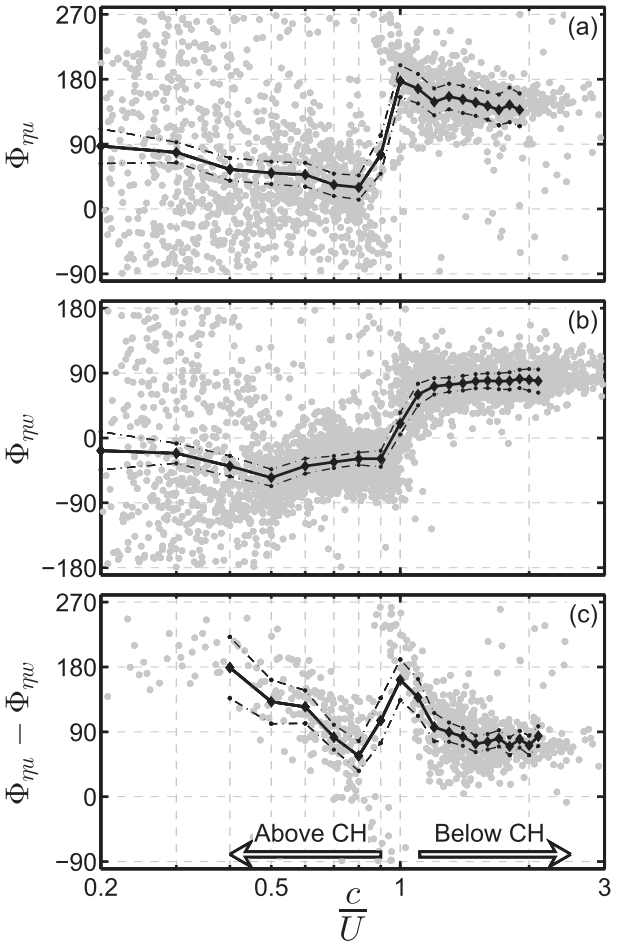

FIG. 7. (a) $\Phi_{\eta u}$. (b) $\Phi_{\eta w}$. (c) Difference between the two phase shifts. Gray dots are the phase shifts for wave ages c/U in which the squared coherence is greater than 0.1. $\gamma^2_{\eta u} > 0.1$ in (a), $\gamma^2_{\eta w} > 0.1$ in (b), and $\gamma^2_{\eta u} > 0.1$ and $\gamma^2_{\eta w} > 0.1$ in (c). The data are from the two anemometers. The diamonds joined by the black solid line are the bin-averaged values with their 95% confidence intervals (black dashed–dotted line with circles).

$$\hat{a} - 2\frac{\sigma}{\sqrt{N}} \le a \le \hat{a} + 2\frac{\sigma}{\sqrt{N}}, \tag{10}$$

where the estimate of the standard deviation is

$$\sigma = \frac{\sqrt{1 - \hat{\gamma}^2_{\eta u_i}}}{|\hat{\gamma}_{\eta u_i}|\sqrt{2}}. \tag{11}$$

The bin-averaged squared coherence between the surface displacement and the velocity fluctuations is $\hat{\gamma}^2_{\eta u_i}$. These figures show that the abrupt change of phase is a robust feature of the wave-induced flow field for a large range of wind–wave conditions. The collapse of the data is remarkable, especially when c/U is greater than unity (i.e., below the critical height). The scatter is large when the wave age c/U is less than unity and becomes larger when the wave age c/U decreases. This can be attributed to the low level of coherence at the scales of the shortest waves, which implies a greater uncertainty for the computed phase shift. The sharp peak of the bin-averaged phase between waves and horizontal velocity that occurs at the critical height ($\Phi_{\eta u}$ reaches about 190° at $c/U = 1$ then tends to 150°–155° for $c/U > 1$) is consistent with the CLT and measurements of Stewart [(1970), their Fig. 9] and Hristov et al. [(2003), their Fig. 3b].

When measurements are performed below the critical height (i.e., $c/U > 1$), the wave-induced horizontal and vertical velocities are almost in quadrature. Thus, the wave-induced momentum flux below the critical height is expected to be very small. However, according to the CLT, the small deviation from the configuration where

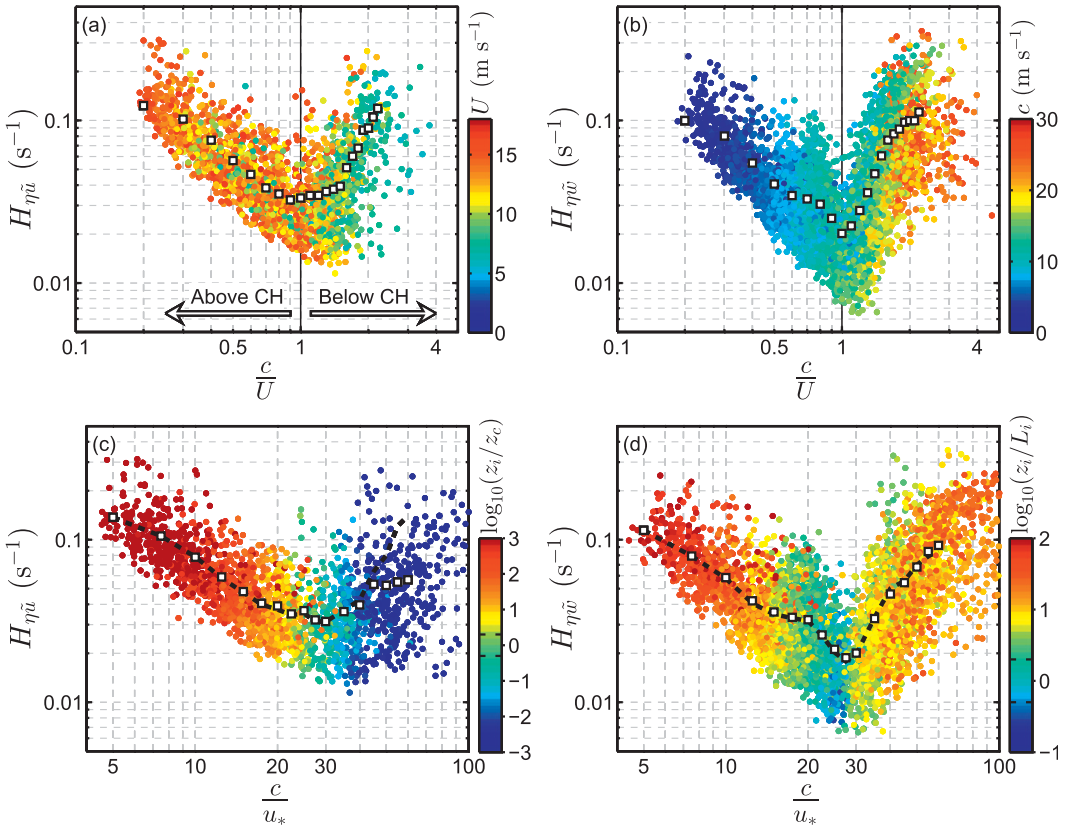

FIG. 8. The scaled amplitude of the wave-induced velocities [Eq. (13)] as a function of wave ages (a),(b) c/U and (c), (d) c/u_*. Scaled horizontal velocity $H_{\eta\tilde{u}}$ in (a),(c) and scaled vertical velocity $H_{\eta\tilde{w}}$ in (b),(d) are shown. The color scale represents the mean wind speed in (a), the phase speed in (b), the ratio of the height of the ECS z_i to the critical height z_c [Eq. (15)] in (c), and the ratio of the height of the ECS z_i to the height of the inner region L_i [Eq. (16)] in (d). The open squares are the bin-averaged values of these scaled wave-induced velocities. The black dashed lines are the bin-averaged values for U_{10} greater than 10 m s^{-1} in (c),(d).

the two velocities are exactly in quadrature is responsible for the transfer of momentum between wind and waves and so is responsible for the wave growth. This departure from the quadrature is shown in Fig. 7c where the bin-averaged phase shift between the horizontal and vertical components of the wind varies from 90° to 70° for wave ages c/U between 1.2 and 2. Hence, these waves are expected to support a part of the wave-induced momentum flux.

Figures 8a–8d show the evolution of the wave-induced velocities scaled by the wave height as function of the spectral wave ages c/U and c/u_*. The wave-induced terms have been computed following the technique described by Veron et al. (2008, 2009). This method uses the coherence and phase between each velocity and the surface displacement. In the following section, we describe this method using the vertical velocity w. The same method has been employed for the horizontal velocity u. By denoting the squared coherence between w and η in the frequency domain by $\gamma^2_{\eta w}$, their relative phase by $\Phi_{\eta w}$, and the spectral density of w by S_{ww}, then the spectral density of the wave-induced fluctuations $\tilde{w}$ is given by $S_{\tilde{w}\tilde{w}} = S_{ww} \times \gamma^2_{\eta w}$. By denoting the cross-spectral density of η and w by $S_{\eta w}$, the transfer function $T_{\eta w}$ is given by $T_{\eta w} = S_{\eta w}/S_{\eta\eta}$, where $S_{\eta\eta}$ is the spectral density of the wave displacement and w is the vertical velocity component defined as the sum of the mean $\overline{w}$ (which is zero for the vertical velocity), the turbulent component w', and the wave-induced component $\tilde{w}$. Thus, the complex transfer function between the wave-induced vertical velocity $\tilde{w}$ and η is given by

$$T_{\eta\tilde{w}} = \frac{S_{\eta w} \times \gamma^2_{\eta w}}{S_{\eta\eta}}. \tag{12}$$

Finally, the scaled amplitude of the wave-induced vertical velocity $H_{\eta\tilde{w}}$ and its phase relative to the surface elevation $\Phi_{\eta\tilde{w}}$ are the amplitude and phase, respectively, of the transfer function $T_{\eta\tilde{w}}$:

$$H_{\eta\tilde{w}} = |T_{\eta\tilde{w}}|, \tag{13}$$

and

$$\Phi_{\eta\tilde{w}} = \arg(T_{\eta\tilde{w}}). \tag{14}$$

For both scaled wave-induced velocities, the collapse of the data points is quite good with both representations (c/U and c/u_*), for data from both anemometers. Both scaled wave-induced velocities decrease in the neighborhood of the critical height. This behavior is consistent with the bimodal distributions of Fig. 6 as well as the CLT. This result is noteworthy given the large range of wind–wave conditions represented. Furthermore, these figures show that the two scaled wave-induced velocities are of the same order of magnitude although $H_{\eta\tilde{u}}$ is slightly larger than $H_{\eta\tilde{w}}$ when $c/U < 1$. This result is in agreement with Hristov et al. [(2003), their Figs. 3a,c].

In Fig. 8a, the color scale represents the mean wind speed U, in Fig. 8b the phase speed c, in Fig. 8c the elevation of the ECS z_i relative to the critical height z_c of waves with phase speed c where

$$z_c = z_i \exp\left\{\frac{\kappa[c - U(z_i)]}{u_*}\right\}, \tag{15}$$

and in Fig. 8d the elevation of the ECS z_i relative to the height of the inner region L_i of waves with phase speed c. The height of the inner region L_i is defined using time scales of the turbulence in the inner and the outer regions (Belcher and Hunt 1998):

$$kL_i|U(L_i) - c| = 2\kappa u_*. \tag{16}$$

Cases where $c/U < 1$ ($c/u_* \lesssim 30$) are mostly representative of high winds ($U > 10\,\mathrm{m\,s^{-1}}$) and slow waves ($c \lesssim 10\,\mathrm{m\,s^{-1}}$), while for $c/U > 1$, the wind–wave conditions are more varied with wind and phase speeds ranging throughout the range of the color scales.

Figures 8c and 8d show that in the range $20 \lesssim c/u_* \lesssim 30$, the height of the ECS, the depth of the inner region and the critical height are of the same order of magnitude ($\frac{1}{2} < z_i/z_c < 2$ and $\frac{1}{2} < z_i/L_i < 2$). According to Belcher and Hunt (1998), this is the transition between the slow and the fast wave regimes, the intermediate regime. When $c/u_* \lesssim 20$, the measurements were performed above the critical layer which sits in the thin inner region; this is the slow wave regime. When $c/u_* \gtrsim 30$, measurements were undertaken above the thin inner region and below the critical layer; this is the fast wave regime.

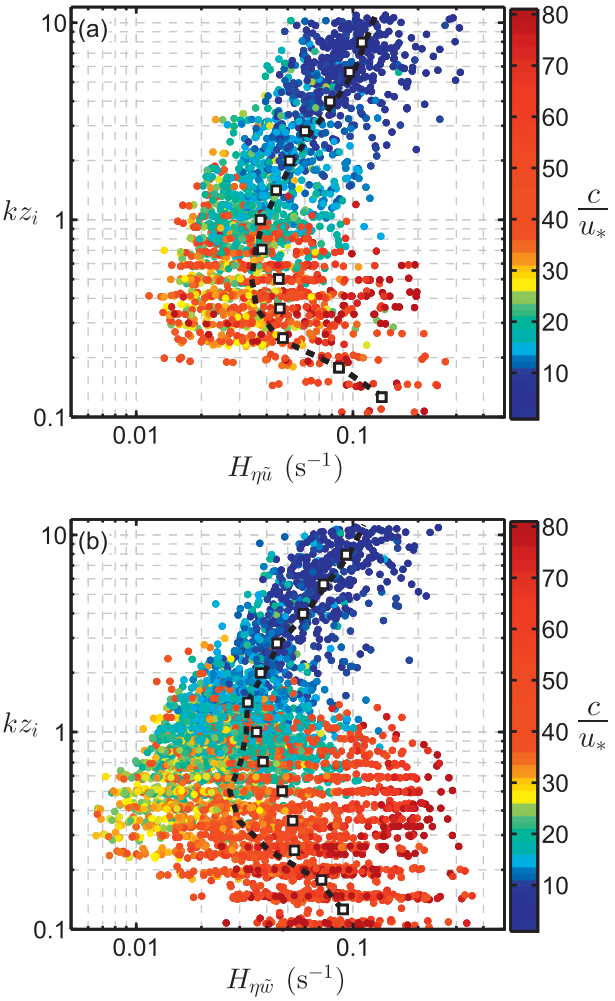

FIG. 9. The scaled amplitude of the wave-induced velocities [Eq. (13)] as a function of the normalized height kz_i. (a) $H_{\eta\tilde{u}}$ and (b) $H_{\eta\tilde{w}}$ are shown. The open squares are the bin-averaged values of these scaled wave-induced velocities. The black dashed lines are the bin-averaged values for U_{10} greater than $10\,\mathrm{m\,s^{-1}}$.

Figure 9 shows the variations of the amplitude of the scaled wave-induced horizontal $H_{\eta\tilde{u}}$ and vertical $H_{\eta\tilde{w}}$ velocities with the spectral normalized height kz_i, where $k = 4\pi^2 f^2/g$. The color scale represents the spectral wave age c/u_*. The open squares are the bin-averaged values when all the data are considered, while the dashed line represents the bin-averaged values for data when U_{10} is greater than $10\,\mathrm{m\,s^{-1}}$. The same bin-average procedures were also applied to the data plotted as a function of the wave age c/u_* (Figs. 8c,d). The difference between these two bin-averaged procedures shows that the use of the spectral normalized height kz_i does not collapse the data for different wind–wave conditions, while the two bin-averaged procedures provide the same values when data are plotted against the spectral wave

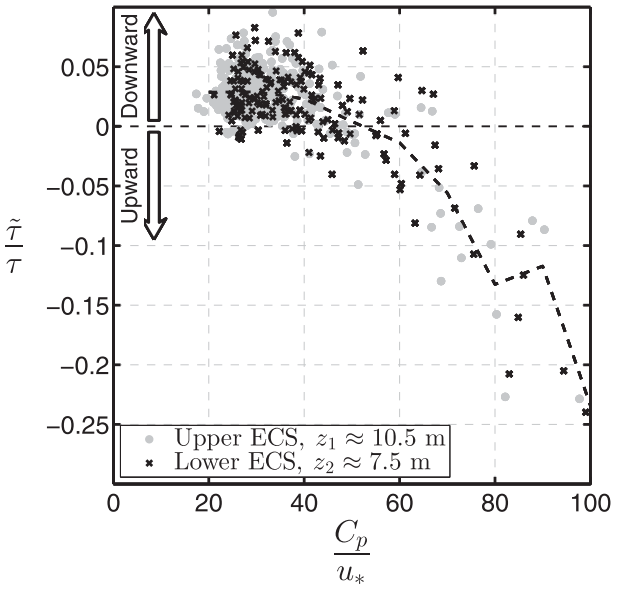

FIG. 10. Contribution of the wave-induced momentum flux $\tilde{\tau} = \rho\overline{\tilde{u}\tilde{w}}$ to the total momentum flux $\tau = \rho\overline{uw}$ as function of the wave age C_p/u_*, where C_p is the phase speed at the peak of the wave spectrum. The black dotted line joins bin-averaged values of the gathered data from both ECSs.

age c/u_* or c/U. Furthermore, the scatter of the data is more than one order of magnitude especially when $kz_i < 1$ (Fig. 9). The scatter is at least 2 or 3 times greater than when the data are plotted as a function of the wave age (Fig. 8). Hence, the comparison between Fig. 8 and Fig. 9 shows that the variations of the amplitude of the scaled wave-induced velocities are primarily driven by the effects of the critical layer before showing any dependence on the normalized height. In that context, we have tried to study the dependence with the normalized height for different ranges of wave ages as was done in Hare et al. (1997). It turned out that the variations of the scaled wave-induced velocities were still mainly attributable to variations of the wave age.

4. Momentum fluxes

Figure 10 shows the dependence of the contribution of the measured wave-induced momentum flux to the total momentum flux $\tilde{\tau}/\tau = \overline{\tilde{u}\tilde{w}}/\overline{uw}$ on the wave age of the dominant waves C_p/u_*. Each point represents a 30-min average. Data from both ECSs are reported; gray solid circles are from the upper ECS and black crosses are from the lower ECS. Data for directions between wind and waves greater than 30° are not reported. Following the decomposition of the wind field into mean $\overline{u}$, turbulent u', and wave-induced $\tilde{u}$ terms as described above, the wave-induced momentum flux $\tilde{\tau}$, which is defined by the product of the air density ρ with the covariance between the wave-induced horizontal and vertical velocities, is computed using the spectra of these velocities and their respective phases with the surface displacement as was done in Veron et al. (2008) and Kihara et al. (2007). Hence, the wave-induced momentum flux is given by

$$\tilde{\tau} = \rho\overline{\tilde{u}\tilde{w}} = \rho\sum_{i}^{N}\sqrt{S_{\tilde{u}\tilde{u}}(f_i)S_{\tilde{w}\tilde{w}}(f_i)}\cos[\Phi_{\eta\tilde{u}}(f_i) - \Phi_{\eta\tilde{w}}(f_i)]\Delta f, \tag{17}$$

where Δf is the frequency resolution and N is the number of segments from the FFT decomposition ($N = 1025$). The discrete frequency is $f_i = i\Delta f$. Later in the text and figures, the subscript i will be omitted for notational simplicity. The (total) momentum flux τ is defined by the product of the air density with the covariance between the horizontal and vertical velocities and can be estimated through the sum of the real part of the discrete cross-spectrum (i.e., the cospectrum Co_{uw}) between the two velocity variables in the frequency domain:

$$\tau = \rho\overline{uw} = \rho\sum^{N}\mathrm{Re}[S_{uw}(f)]\Delta f = \rho\sum^{N}\mathrm{Co}_{uw}(f)\Delta f. \tag{18}$$

For the dataset analyzed, the total momentum flux τ remained negative (i.e., downward). Hence, a positive value of the contribution $\tilde{\tau}/\tau$ means that the wave-induced momentum flux is directed toward the surface, while $\tilde{\tau}/\tau < 0$ means that $\tilde{\tau}$ is from the waves to the wind.

Figure 10 shows that the wave-induced momentum flux supported by scales quantifiable at the height of the anemometers represents a small part of the total momentum flux (less than 10%) and is directed toward the surface when the wave age C_p/u_* is less than about 40 (which corresponds to C_p/U_{10} smaller than 1.2–1.4). The wave-induced momentum flux measured at a fixed distance MSL for a wave field with a broad band spectrum, as in this experiment, depends on the vertical gradient of each spectral component of this flux. To quantify the order of magnitude of the scales that support the measured wave-induced momentum flux, we have computed, for each spectral component, the time-averaged values of the squared coherence between the surface displacement and both the horizontal and vertical components of the wind, $\langle\gamma^2_{\eta u}(f)\rangle = n^{-1}\sum_j^n\gamma^2_{\eta u}(j,f)$ and $\langle\gamma^2_{\eta w}(f)\rangle = n^{-1}\sum_j^n\gamma^2_{\eta w}(j,f)$, where n is the number of 30-min samples and angle brackets denote an ensemble average. Both of these averaged squared coherences presents a maximum around 0.1 Hz, and becomes small (almost 10 times smaller than their maximum values) when the

frequency is greater than 0.3 Hz. This result indicates that above 0.3 Hz the fluctuations of the velocities are not correlated with the wave field and that the wave-induced momentum flux we measured is mainly supported by waves of wavelengths longer than approximately 15 m. Thus, assuming that the wave-induced momentum flux supported by waves longer than approximately 15 m keeps its surface amplitude up to the heights of the anemometer, then Fig. 10 shows that about 95% of the momentum flux is transferred to the wave field via waves with wavelengths shorter than approximately 15 m. This is in accordance with the conclusion of Makin et al. (1995), Makin and Kudryavtsev (1999), and Donelan (1998), who found that, for fully developed and developing seas, about 80%–90% of the form drag is supported by short waves with wavelengths less than $O(10)$ m.

When the wave age C_p/u_* is greater than 40, the wave-induced momentum flux changes sign and its contribution begins to be a significant part of the total momentum flux (its amplitude can represent up to 20% of the amplitude of the total momentum flux for the oldest waves). In that case, even if the total momentum flux remains negative (downward), the long waves support a counterpart directed upward. Such behavior has been observed in the field for conditions of low wind blowing over swell (Antonia and Chambers 1980; Grachev and Fairall 2001; Högström et al. 2009).

Further analysis of the scales responsible for the measured wave-induced momentum flux $\tilde{\tau}$ was undertaken by investigating the dependence of its spectral components $\Delta\tilde{\tau}(f)$ on the spectral wave age $c(f)/U = g/(2\pi fU)$. The spectral wave-induced momentum flux $\Delta\tilde{\tau}(f)$ is defined by the product of the air density with the wave-induced cospectrum integrated from f to $f + \Delta f$, where Δf is the frequency resolution increment:

$$\Delta\tilde{\tau}(f) = \rho\int_{f}^{f+\Delta f} \mathrm{Co}_{\tilde{u}\tilde{w}}(\zeta)\,d\zeta = \rho\mathrm{Co}_{\tilde{u}\tilde{w}}(f)\Delta f. \quad (19)$$

The wave-induced cospectrum is the real part of the cross spectrum between the wave-induced horizontal and vertical velocities of the wind supported by frequencies in the range $(f, f + \Delta f)$. Following the definition of the wave-induced momentum flux expressed in Eq. (17), the wave-induced cospectrum is expressed as follows:

$$\mathrm{Co}_{\tilde{u}\tilde{w}}(f) = \mathrm{Re}[S_{\tilde{u}\tilde{w}}(f)] = \sqrt{S_{\tilde{u}\tilde{u}}(f)S_{\tilde{w}\tilde{w}}(f)}\cos[\Phi_{\eta\tilde{u}}(f) - \Phi_{\eta\tilde{w}}(f)]. \quad (20)$$

For each 30-min sample, the wave-induced momentum flux $\tilde{\tau}$ is equal to the sum of all its spectral components $\Delta\tilde{\tau}(f)$:

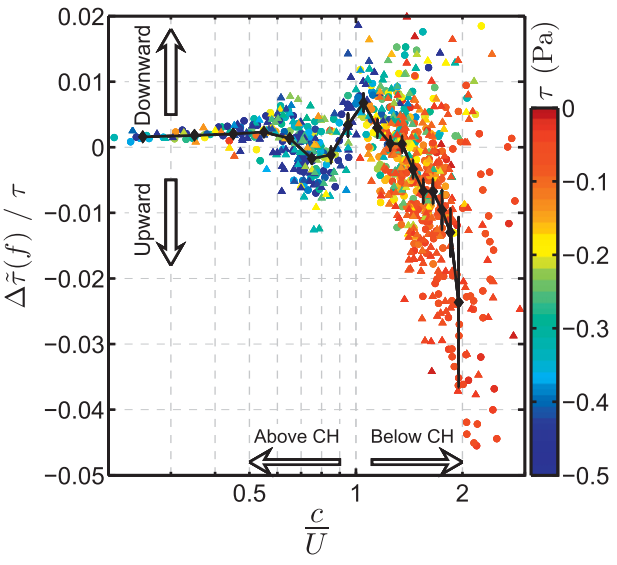

FIG. 11. Contribution of $\Delta\tilde{\tau}(f) = \rho\mathrm{Co}_{\tilde{u}\tilde{w}}(f)\Delta f$ to $\tau = \rho\overline{uw}$ as a function of c/U for selected data with both $\gamma^2_{\eta u} > 0.1$ and $\gamma^2_{\eta w} > 0.1$. Solid circles (solid triangles) are data from upper (lower) ECS. Black solid diamonds joined by the black line represent bin-averaged values of the gathered data with their corresponding 95% confidence intervals.

$$\tilde{\tau} = \sum^{N}\Delta\tilde{\tau}(f) = \int d\tilde{\tau}(f) = \int\frac{d\tilde{\tau}(f)}{df}df \quad \text{as} \quad N \to \infty. \quad (21)$$

Figure 11 presents the dependence of the spectral contributions of the wave-induced momentum flux to the total momentum flux $\Delta\tilde{\tau}(f)/\tau$ on the spectral wave age c/U. The magnitude of the spectral contribution of the wave-induced momentum flux is smaller for younger waves. Furthermore, the spectral contribution from the fast waves is opposed to the downward momentum flux, meaning that the contribution of waves traveling faster than the wind represents an upward flux. For waves traveling slower than the wind, there is no evident trend in the data because the bin-averaged values are close to zero within the scatter of the limited dataset. Nevertheless, a change of sign of the bin-averaged spectral contribution appears just above the critical layer ($0.7 < c/U < 0.9$). In the following section, we will discuss how this pattern can be interpreted.

5. Discussion and conclusions

We have conducted measurements of the coherent wind field above waves in relatively strong wind and wave conditions ($H_s \leq 5$ m and $U_{10} > 15\,\mathrm{m\,s^{-1}}$), where the wave-induced fluctuations were extracted through a simple method of analysis. Although there was a high level of turbulence in the airflow, we were able to

compute wave-induced fluctuations with amplitudes less than $O(0.1)\,\mathrm{m\,s^{-1}}$. The spectral analysis permitted us to study the wind–wave interactions over a wide range of scales and to provide the resolution of the spectral components of wave-coherent structures in the airflow, as a function of spectral dimensionless parameters such the wave ages, $c(f)/U$ and $c(f)/u_*$, based on the phase speed $c(f)$ of the waves.

We showed the existence of a sharp change of phase between the wave-induced components of the wind and the surface displacement at the critical height. This behavior, predicted by the CLT, is robust, appears to be valid for all the wave scales studied ($0.05 < f < 0.3\,\mathrm{Hz}$), and is observed for both horizontal and vertical velocity components. This result is well represented by Fig. 7 where the data are ordered as a function of the spectral wave age c/U.

As shown in Fig. 5, the vertical velocity is found to be more coherent with the waves than the horizontal velocity. This result is in accordance with the previous observations of Hsu et al. [(1982), their Fig. 6] for young waves and Drennan et al. (1999) for fast-moving waves. However, in our case, the wave-induced velocities scaled by the wave height are of the same order of magnitude (Fig. 8). For both velocity components, a decrease of the coherence is observed when the phase speed equals the wind speed, with the wave-induced velocities almost vanishing at the critical height. This result is reinforced by the data in Figs. 7 and 8, which show the sharp change of behavior of the wave-induced fluctuations, both in amplitude and phase, in the neighborhood of the critical height. These results provide three different sets of experimental evidence of the effects of the critical layer on the airflow. Moreover, we showed that the use of the spectral wave ages c/U and c/u_* collapses the data much better than the spectral normalized height kz_i. This implies that the variations of the amplitude of the scaled wave-induced velocities are more influenced by the effect of the critical layer than variations of the normalized height. These findings are qualitatively consistent with the laboratory experiments of Stewart (1970), with the field data of Hristov et al. (2003), and with the DNS of Kihara et al. (2007) and Sullivan et al. (2000), although Sullivan et al. (2000) found that the wave-induced streamwise component varies more smoothly across the critical height than the wave-induced vertical component. Note that in Sullivan et al. (2000) the streamwise-integrated wave-correlated fields are computed at a constant distance above the instantaneous wavy surface, while our measurements are at a constant height MSL.

We showed that, for mature seas ($C_p/u_* > 40$, $C_p/U_{10} > 1.5$), the wave-induced momentum flux $\tilde{\tau}$ measured approximately 10 m MSL is upward and its amplitude can represent up to 20% of the amplitude of the total downward momentum flux (Fig. 10). This is consistent with previous observations from Grachev and Fairall (2001) and Smedman et al. (1999, 2009), and is qualitatively consistent with numerical simulations of Sullivan et al. (2008), Hanley and Belcher (2008), and Makin (2008), who showed that under light winds ($U < 2\,\mathrm{m\,s^{-1}}$), long ocean waves (swell) cause an upward momentum flux. In our case, for the largest wave ages, the mean wind speed remains greater than $6\,\mathrm{m\,s^{-1}}$, and the total momentum flux remains negative (downward). This implies that the upward wave-induced momentum flux supported by the long waves is not strong enough to balance the downward momentum flux mostly supported by shorter scales of the turbulence that transfers momentum to the youngest waves of the wave field.

Moreover, from developing to fully developed seas, when the dominant wave age C_p/u_* encompasses the range 20–40 ($0.8 < C_p/U_{10} < 1.5$), the wave-induced momentum flux is mainly downward and the values measured at the heights of the ECSs represent less than 5%–10% of the total wind stress. According to the level of coherence observed between the airflow velocities and the displacement of the surface, the wave-induced momentum flux measured at the height of the ECSs is only supported by waves with wavelengths greater than approximately 15 m. Hence, assuming that the wave-induced momentum flux supported by these long waves is approximately constant between the heights of the ECSs and the surface, it demonstrates that more than 90% of the momentum flux is supported by waves smaller than approximately 15 m. This is in accordance with numerical results from Makin et al. (1995) and the conclusions of Donelan (1998).

When measurements are undertaken above the critical height ($c/U < 1$), the spectral wave-induced momentum flux $\Delta\tilde{\tau}(f)$ does not fully vanish, even if it tends to zero for the youngest waves (Fig. 11). It also shows that there is a change of sign just above the critical height where a fraction of the waves traveling slower than the wind (when $0.7 < c/U < 0.9$, which corresponds to waves such that $15 < c/u_* < 30$) supports an upward wave-induced momentum flux. Such a pattern is not described by the critical layer theory in which the wave-induced momentum flux is zero above the critical height and is downward and constant below the critical height. A divergence of results between the theory and measurements is not surprising because the critical layer theory neglects some aspects of the airflow (e.g., viscous effects and perturbations of the Reynolds stress due to the presence of waves). It means that other phenomena need to be taken into account to fully describe the airflow, especially in the vicinity of the critical layer. For example,

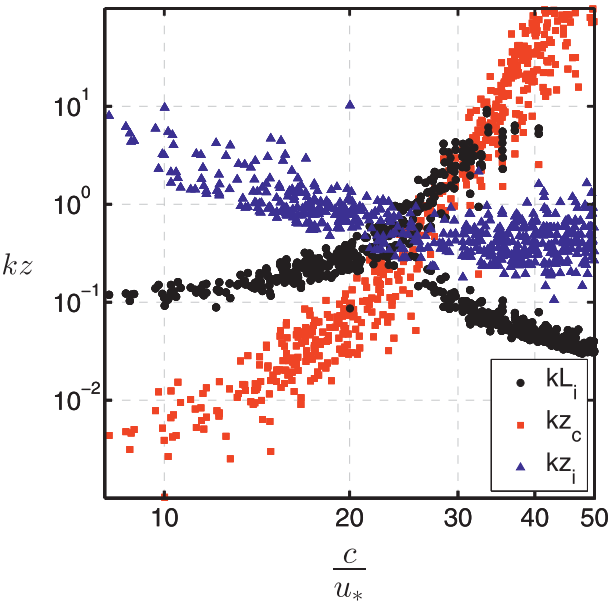

FIG. 12. Variations with the spectral wave age c/u_* of the normalized inner-region height kL_i (black dots), critical height kz_c (red squares), and height of measurement kz_i (blue triangles). Each height (L_i, z_c, and z_i) is normalized by the wavenumber $k = g/c^2$ of waves propagating at the phase speed c. In the range $20 < c/u_* < 30$, these heights are of the same order of magnitude.

the numerical study by Townsend (1972), where the perturbations of the Reynolds stress by the waves are modeled, showed that the wave-induced momentum flux significantly varies with height and can oscillate (change sign) before vanishing far above the waves. In our case, the waves traveling slower than the wind, which support an upward wave-induced momentum flux above the critical height, are in the range $15 < c/u_* < 30$; that is, in the intermediate wave regime. Figure 12 shows the dependence on the spectral wave age c/u_* of the normalized height of the inner region kL_i, the normalized critical height kz_c, and the normalized height of measurement kz_i. When $15 < c/u_* < 20$, the height of the inner region approaches the height of measurement while the critical layer approaches the top of the inner region. But in the range $20 < c/u_* < 30$, all these heights are of the same order of magnitude. Belcher and Hunt (1998) advocate that, for the intermediate regime, the shift of the wave-coherent pressure resulting from the positive asymmetry of the streamlines induced by the nonseparated sheltering at heights where the wind blows in the same direction as the waves propagate (above the critical height) can be balanced by the negative asymmetry induced by the reverse flow (below the critical height). Such a balance could be an explanation of the change of sign of the spectral wave-induced momentum flux we observed. Note that the models developed by Belcher and Hunt (1993) for slow waves and Cohen and Belcher (1999) for fast waves, derive solutions of the wind–wave interaction only when the inner region is a thin layer ($kL_i \ll 1$). For the intermediate regime, the inner region is thick and the critical height is of the same order of magnitude as the depth of the inner region, and the solutions derived by these models are not valid.

The numerical simulations from Sullivan et al. [(2000), their Figs. 18 and 19] and Kihara et al. [(2007), their Fig. 8] show that, for monochromatic waves, the vertical profile of the averaged wave-induced momentum flux presents a change of sign associated with the presence of the critical layer with a positive flux above the critical height. The analysis done here is not the same as that performed in the DNS, because in our case, the wave field is broad banded: the data presented in Fig. 11 characterize the spectral contribution of wave-induced momentum flux, and the vertical dependence cannot be computed. Nevertheless, both studies show the existence of an upward wave-induced momentum flux just above the critical height, when the critical layer sits in the top of the inner region, as observed in this study.

Although the present analysis is primarily focused on the linear coupling between the velocity components of the airflow and the wave field and how these wave-coherent velocities are consistent with available theories, such as those of Miles or Belcher and Hunt, other phenomena, such as the effects of wave-breaking (e.g., separation) and nonlinear wave–wave interactions (e.g., effective roughness of shorter waves modulated by longer waves), may affect the airflow, and therefore the measured wave-induced momentum flux. However, the effects of these processes are contained in the analysis of the marine atmospheric boundary layer data as the nonlinear wave–wave interactions and breaking processes contribute to the measured wave field, thus they are implicitly included in the data and its analysis. Hence, if these effects are coherent with the waves, they are effectively included in this analysis, otherwise they are not considered.

A final comment concerns the measurements performed at heights around 10 m MSL. As shown in Fig. 4, the drag coefficient $C_{D_{10}} = (u_*/U_{10})^2$ mainly ranges between 10^{-3} and 2.10^{-3}. As the critical height for waves with phase speed c is defined where the wind speed equals the phase speed of these waves [$c/U(z) = 1$], when measurements are realized around 10 m, the location of the critical height is defined when the ratio c/u_* ranges between 20 and 30:

$$\left.\begin{array}{c} 10^{-3} \lesssim C_{D_{10}} \lesssim 2.10^{-3} \\ c/U(z \approx 10) = 1 \end{array}\right\} \Rightarrow 20 \lesssim c/u_* \lesssim 30. \quad (22)$$

However, the range $20 \lesssim c/u_* \lesssim 30$ also characterizes the intermediate wave regime, which marks the transition between the slow wave regime, where waves grow under the action of the wind, and the fast wave regime, where the waves are attenuated by the wind. It means that values of c/u_* in the range 20–30 represent both a change of the wave regime and a crossing of both the critical layer and the top of the inner region. Thus, in this experimental configuration, it is not trivial to separate the effect of the change of wind–wave regime, the effects of the critical height, and the inner region in the analysis of the data. Measurements performed closer to the surface would help to resolve these issues.

Furthermore, as pointed out by Kihara et al. (2007), the critical values of c/u_*, which separate the three different wind–wave regimes, are derived from the depth of the inner region L_i. But, this parameter is determined using time scales of the turbulence in both the inner and outer regions. This approach has been criticized by Janssen (2004), who shows that, in a logarithmic wind profile, the use of the eddy-turnover time scale as the time scale of the turbulence can give a momentum transfer time scale too small by an order of magnitude. This would lead to an overestimation of the depth of the inner region. In the inner region, the flow is supposed to be in local equilibrium, that is, the advection of the turbulent kinetic energy (TKE) is small compared to the rate of dissipation of the TKE; in the outer region, the advection of the TKE needs to be taken into account to close the TKE budget. In that context, an estimate of the depth of the inner region based on the ratio of the advection of the TKE to the rate of dissipation of the TKE would be more appropriate than the time-scale arguments used to derive Eq. (16).

Acknowledgments. We thank Tom Golfinos and the crew of the R/P *FLIP* for their tireless support of this research in difficult conditions at sea, and Capt. Bill Gaines for his logistical support of R/P *FLIP* operations. The measurements would not have been possible without the work of Fabrice Veron, Peter Sutherland, and Nick Statom during the experiment. This research was supported by funding to WKM from the Office of Naval Research (Physical Oceanography) as part of the HiRes Air–Sea Interaction Departmental Research Initiative (HiRes DRI).

REFERENCES

Antonia, R. A., and A. J. Chambers, 1980: Wind–wave-induced disturbances in the marine surface layer. *J. Phys. Oceanogr.,* **10,** 611–622.

Belcher, S. E., and J. C. R. Hunt, 1993: Turbulent shear flow over slowly moving waves. *J. Fluid Mech.,* **251,** 109–148.

——, and ——, 1998: Turbulent flow over hills and waves. *Annu. Rev. Fluid Mech.,* **30,** 507–538.

Bendat, J. S., and A. G. Piersol, 2010: *Random Data Analysis and Measurement Procedures.* 4th ed. Wiley and Sons, 640 pp.

Benjamin, T. B., 1959: Shearing flow over a wavy boundary. *J. Fluid Mech.,* **6,** 161–205.

Bole, J. B., and E. Y. Hsu, 1969: Response of gravity water waves to wind excitation. *J. Fluid Mech.,* **35,** 657–675.

Chalikov, D. V., 1978: The numerical simulation of wind–wave interaction. *J. Fluid Mech.,* **87,** 561–582.

Cohen, J. E., and S. E. Belcher, 1999: Turbulent shear flow over fast-moving waves. *J. Fluid Mech.,* **386,** 345–371.

Davidson, K. L., and A. J. Frank, 1973: Wave-related fluctuations in the airflow above natural waves. *J. Phys. Oceanogr.,* **3,** 102–119.

Davis, R. E., 1970: On the turbulent flow over a wavy boundary. *J. Fluid Mech.,* **42,** 721–731.

Dobson, F. W., 1971: Measurements of atmospheric pressure on wind-generated sea waves. *J. Fluid Mech.,* **48,** 91–127.

Donelan, M. A., 1998: *Air–Water Exchange Processes. Geophys. Monogr.,* Vol. 54. Amer. Geophys. Union, 19–36.

——, A. V. Babanin, I. R. Young, and M. L. Banner, 2006: Wave-follower field measurements of the wind-input spectral function. Part II: Parameterization of the wind input. *J. Phys. Oceanogr.,* **36,** 1672–1689.

Drennan, W. M., K. K. Kahma, and M. A. Donelan, 1999: On momentum flux and velocity spectra over waves. *Bound.-Layer Meteor.,* **92,** 489–515.

Edson, J. B., A. A. Hinton, K. E. Prada, J. E. Hare, and C. W. Fairall, 1998: Direct covariance flux estimates from mobile platforms at sea. *J. Atmos. Oceanic Technol.,* **15,** 547–562.

Fairall, C. W., E. F. Bradley, J. E. Hare, A. A. Grachev, and J. B. Edson, 2003: Bulk parameterization of air–sea fluxes: Updates and verification for the COARE algorithm. *J. Climate,* **16,** 571–591.

Gent, P. R., and P. A. Taylor, 1976: A numerical model of the air flow above water waves. *J. Fluid Mech.,* **77,** 105–128.

Grachev, A. A., and C. W. Fairall, 2001: Upward momentum transfer in the marine boundary layer. *J. Phys. Oceanogr.,* **31,** 1698–1711.

Grare, L., W. L. Peirson, H. Branger, J. W. Walker, J.-P. Giovanangeli, and V. Makin, 2013: Growth and dissipation of wind-forced, deep-water waves. *J. Fluid Mech.,* **722,** 5–50.

Hanley, K. E., and S. E. Belcher, 2008: Wave-driven wind jets in the marine atmospheric boundary layer. *J. Atmos. Sci.,* **65,** 2646–2660.

Hara, T., and S. E. Belcher, 2002: Wind forcing in the equilibrium range of wind–wave spectra. *J. Fluid Mech.,* **470,** 223–245.

Hare, J. E., T. Hara, J. B. Edson, and J. M. Wilczak, 1997: A similarity analysis of the structure of airflow over surface waves. *J. Phys. Oceanogr.,* **27,** 1018–1037.

Hasselmann, D., and J. Bosenberg, 1991: Field measurements of wave-induced pressure over wind–sea and swell. *J. Fluid Mech.,* **230,** 391–428.

Högström, U., A. Smedman, E. Sahlée, W. M. Drennan, K. K. Kahma, H. Pettersson, and F. Zhang, 2009: The atmospheric boundary layer during swell: A field study and interpretation of the turbulent kinetic energy budget for high wave ages. *J. Atmos. Sci.,* **66,** 2764–2779.

——, A. Rutgersson, E. Sahlée, A.-S. Smedman, T. Hristov, W. Drennan, and K. Kahma, 2013: Air–sea interaction features in the Baltic Sea and at a Pacific trade wind site: An intercomparison study. *Bound.-Layer Meteor.,* **147,** 139–163.

Hristov, T. S., S. D. Miller, and C. A. Friehe, 2003: Dynamical coupling of wind and ocean waves through wave-induced air flow. *Nature,* **422,** 55–58.

Hsiao, S. V., 1983: Measurements of wind velocity and pressure with a wave follower during Marsen. *J. Geophys. Res.,* **88** (C14), 9841–9849.

Hsu, C.-T., and E. Y. Hsu, 1983: On the structure of turbulent flow over a progressive water wave: Theory and experiment in a transformed wave-following coordinate system. Part 2. *J. Fluid Mech.,* **131,** 123–153.

——, ——, and R. L. Street, 1981: On the structure of turbulent flow over a progressive water wave: Theory and experiment in a transformed, wave-following coordinate system. *J. Fluid Mech.,* **105,** 87–117.

——, H.-Y. Wu, E.-Y. Hsu, and R. L. Street, 1982: Momentum and energy transfer in wind generation of waves. *J. Phys. Oceanogr.,* **12,** 929–951.

Janssen, P., 2004: *The Interaction of Ocean Waves and Wind.* Cambridge University Press, 308 pp.

Kato, H., and K. Sano, 1969: Measurements of wind velocity fluctuations over waves in a wind–wave tunnel. Port and Airport Research Institute Tech. Rep. 1, 35 pp.

Kihara, N., H. Hanazaki, T. Mizuya, and H. Ueda, 2007: Relationship between airflow at the critical height and momentum transfer to the traveling waves. *Phys. Fluids,* **19,** 015102, doi:10.1063/1.2409736.

Kondo, J., Y. Fujinawa, and G. Naito, 1972: Wave-induced wind fluctuation over the sea. *J. Fluid Mech.,* **51,** 751–771.

Lai, R. J., and O. H. Shemdin, 1971: Laboratory investigation of air turbulence above simple water waves. *J. Geophys. Res.,* **76,** 7334–7350.

Makin, V., 2008: On the possible impact of a following-swell on the atmospheric boundary layer. *Bound.-Layer Meteor.,* **129,** 469–478.

——, and V. N. Kudryavtsev, 1999: Coupled sea surface–atmosphere model 1. Wind over waves coupling. *J. Geophys. Res.,* **104** (C4), 7613–7623.

——, ——, and C. Mastenbroek, 1995: Drag of the sea surface. *Bound.-Layer Meteor.,* **73,** 159–182.

Massel, S., and R. Brinkman, 1998: On the determination of directional wave spectra for practical applications. *Appl. Ocean Res.,* **20,** 357–374.

Mastenbroek, C., V. K. Makin, M. H. Garat, and J. P. Giovanangeli, 1996: Experimental evidence of the rapid distortion of turbulence in the air flow over water waves. *J. Fluid Mech.,* **318,** 273–302.

Miles, J. W., 1957: On the generation of surface waves by shear flows. *J. Fluid Mech.,* **3,** 185–204.

——, 1959: On the generation of surface waves by shear flows. Part 2. *J. Fluid Mech.,* **6,** 568–582.

——, 1993: Surface-wave generation revisited. *J. Fluid Mech.,* **256,** 427–441.

Mitsuyasu, H., and T. Honda, 1982: Wind-induced growth of water waves. *J. Fluid Mech.,* **123,** 425–442.

Monin, A., and A. Obukhov, 1954: Basic laws of turbulent mixing in the surface layer of the atmosphere (in Russian). *Tr. Geofiz. Inst., Akad. Nauk SSSR,* **24,** 163–187.

Panofsky, H. A., 1963: Determination of stress from wind and temperature measurements. *Quart. J. Roy. Meteor. Soc.,* **89,** 85–94.

Papadimitrakis, Y. A., E. Y. Hsu, and R. L. Street, 1984: On the structure of the velocity field over progressive mechanically-generated water waves. *J. Phys. Oceanogr.,* **14,** 1937–1948.

——, ——, and ——, 1986: The role of wave-induced pressure fluctuations in the transfer processes across an air–water interface. *J. Fluid Mech.,* **170,** 113–137.

Peirson, W. L., and A. W. Garcia, 2008: On the wind-induced growth of slow water waves of finite steepness. *J. Fluid Mech.,* **608,** 243–274.

Plant, W. J., 1982: A relationship between wind stress and wave slope. *J. Geophys. Res.,* **87** (C3), 1961–1967.

Savelyev, I. B., B. K. Haus, and M. A. Donelan, 2011: Experimental study on wind–wave momentum flux in strongly forced conditions. *J. Phys. Oceanogr.,* **41,** 1328–1344.

Shemdin, O. H., and E. Y. Hsu, 1967: Direct measurement of aerodynamic pressure above a simple progressive gravity wave. *J. Fluid Mech.,* **30,** 403–416.

Smedman, A., U. Högström, H. Bergström, A. Rutgersson, K. K. Kahma, and H. Pettersson, 1999: A case study of air–sea interaction during swell conditions. *J. Geophys. Res.,* **104** (C11), 25 833–25 851.

——, X. G. Larsén, U. Högström, K. K. Kahma, and H. Pettersson, 2003: Effect of sea state on the momentum exchange over the sea during neutral conditions. *J. Geophys. Res.,* **108,** 3367, doi:10.1029/2002JC001526.

——, U. Högström, E. Sahlée, W. M. Drennan, K. K. Kahma, H. Pettersson, and F. Zhang, 2009: Observational study of marine atmospheric boundary layer characteristics during swell. *J. Atmos. Sci.,* **66,** 2747–2763.

Smith, J. A., and K. F. Rieder, 1997: Wave-induced motion of flip. *Ocean Eng.,* **24,** 95–110.

Snyder, R. L., F. W. Dobson, J. A. Elliott, and R. B. Long, 1981: Array measurements of atmospheric pressure fluctuations above surface gravity waves. *J. Fluid Mech.,* **102,** 1–59.

Stewart, R. H., 1970: Laboratory studies of the velocity field over deep-water waves. *J. Fluid Mech.,* **42,** 733–754.

Sullivan, P. P., J. C. McWilliams, and C.-H. Moeng, 2000: Simulation of turbulent flow over idealized water waves. *J. Fluid Mech.,* **404,** 47–85.

——, J. B. Edson, T. Hristov, and J. C. McWilliams, 2008: Large-eddy simulations and observations of atmospheric marine boundary layers above nonequilibrium surface waves. *J. Atmos. Sci.,* **65,** 1225–1245.

——, J. C. Mc Williams, and T. Hristov, 2010: Large eddy simulation of high wind marine boundary layers above a spectrum of resolved moving waves. Preprints, *19th Symp. on Boundary Layers and Turbulence,* Keystone, CO, Amer. Meteor. Soc., 4B.4. [Available online at https://ams.confex.com/ams/19Ag19BLT9Urban/techprogram/paper_172658.htm.]

Townsend, A. A., 1972: Flow in a deep turbulent boundary layer over a surface distorted by water waves. *J. Fluid Mech.,* **55,** 719–735.

Veron, F., W. K. Melville, and L. Lenain, 2008: Wave-coherent air–sea heat flux. *J. Phys. Oceanogr.,* **38,** 788–802.

——, ——, and ——, 2009: Measurements of ocean surface turbulence and wave-turbulence interactions. *J. Phys. Oceanogr.,* **39,** 2310–2323.

WAFO-Group, cited 2000: WAFO—A MATLAB toolbox for analysis of random waves and loads—A tutorial. Department of Mathematical Statistics, Centre for Mathematical Sciences, Lund University. [Available online at http://www.maths.lth.se/matstat/wafo/.]

Webb, E. K., G. I. Pearman, and R. Leuning, 1980: Correction of flux measurements for density effects due to heat and water vapour transfer. *Quart. J. Roy. Meteor. Soc.,* **106,** 85–100.

Wilson, W. S., M. L. Banner, R. J. Flower, J. A. Michael, and D. G. Wilson, 1973: Wind-induced growth of mechanically generated water waves. *J. Fluid Mech.,* **58,** 435–460.